AIAA JOURNAL
Vol. 46, No. 10, October 2008

Aerodynamic Analysis of an Iced Airfoil at Medium/High Reynolds Number

C. Marongiu,* P. L. Vitagliano,† and G. Zanazzi‡
Italian Center for Aerospace Research (CIRA), 81043 Capua, Italy
and
R. Narducci§
The Boeing Company, Philadelphia, Pennsylvania 19142-0858

DOI: 10.2514/1.34550

The flowfield of the NLF-0414 airfoil with a prescribed ice shape is characterized with numerical solutions to the Navier–Stokes equations. Three flow solvers are used: ZEN, a code developed at CIRA, FLUENT, a commercially available code, and CFL3D, a NASA developed solver. For each code two turbulence models are selected: the Spalart–Allmaras and the shear stress transport κ–ω model. An effort is devoted to ascertain the degree of uncertainty among the numerical codes and turbulence models. Integrated forces and pressure coefficient distributions are compared among the analytic solutions and with available experimental data. The conditions include a range of incidence angles covering pre- and poststall for a freestream Mach number and a Reynolds number of 0.21 and 4.6×10^6, respectively. Generally, steady-state solutions are obtained; however, unsteady solutions are acquired for the highest angles of attack.

Nomenclature

c	=	chord
c_d	=	drag coefficient
c_l	=	lift coefficient
c_m	=	pitching moment coefficient
c_p	=	pressure coefficient
Re	=	Reynolds number
u	=	velocity component in the chordwise direction
x	=	distance along the chord
α	=	angle of attack
Δ	=	change
$()_\infty$	=	freestream conditions

I. Introduction

ICE accretion on lifting surfaces represents an austere situation in the operation of an aircraft producing several important icing regulations to ensure maintainability, reliability, and safety. Ice accretion occurs on many aircraft parts such as the fuselage nose section, engine air intakes, air data systems, and control surfaces. A dangerous effect is on the wing leading edge causing a significant reduction in maximum lift coefficient and, as a consequence, increasing (decreasing) the stall velocity (angle). This motivates the large research effort in the ice accretion prediction using both experimental and numerical instruments. Further, proper ice protection systems have been developed to control and prevent icing formation on critical aircraft systems. In synthesis, ice accretion research tries to supply reliable answers to the following fundamental questions:

1) Where will the ice shape form and to what extent?
2) What are the consequences on the aerodynamic performance?

The first question requires the capability to correctly predict ice formation once thermofluid dynamic properties of the flow are known. The second, instead, implies adequate numerical (or experimental) tools to obtain aerodynamic data for iced geometries. These two points are usually treated sequentially due to the high complexity of the phenomenology. Once the shape is computed (or measured), the aerodynamic degradation is evaluated with respect to the clean configuration.

A collaborative effort between the Italian Center for Aerospace Research (CIRA) and The Boeing Company, begun in 2004 [1], has been conducted to test and validate numerical codes in the prediction of aerodynamic performance for iced airfoils. Of particular interest is the capability of Reynolds-averaged Navier–Stokes (RANS) methods to predict the flow characteristics in such conditions. The test geometry considered here is the natural laminar flow general aviation NLF-0414 airfoil [2]. Ice accumulation and force measurements were made in the Icing Research Tunnel (IRT) at the NASA John H. Glenn Research Center at Lewis Field and documented in [3]. Certain operating conditions yielded a typical glaze ice shape, characterized by two large horns near the leading edge. Because of the high level of turbulence in the IRT, the aerodynamic measurements were repeated in the NASA Langley Research Center Low Turbulence Pressure Tunnel (LTPT) using two fabricated shapes, 623-3D and 623-2D. The latter is a two-dimensional smoothed representation of the real ice shape and has been considered the nominal geometry in the present numerical simulations. The computational fluid dynamics (CFD) analyses for iced geometries exhibit the following peculiarities:

1) The true iced geometry is not well defined due to the presence of jagged contours. Nominal geometry is usually interpolated to have a continuous description. The interpolated curve determines a new and nonphysical geometry that is a potential source of uncertainty.

2) The grid spacing along the airfoil contour must be small enough to reproduce the surface irregularities. As a consequence, greater grid density is required than for standard airfoil analyses.

3) Large hornlike features are formed at the leading edge of glaze ice accretion cases. The flow typically separates at small incidence angles and the aerodynamic behavior is no longer linear. CFD prediction of flows characterized by large separated regions strongly depends on resolving unsteady behavior and modeling turbulence.

Presented as Paper 4283 at the 25th AIAA Applied Aerodynamics Conference, Miami, FL, 25–28 June 2007; received 14 September 2007; revision received 31 January 2008; accepted for publication 12 March 2008.

*Research Engineer, Computational Fluid Dynamics Laboratory. Member AIAA.
†Research Engineer, Computational Fluid Dynamics Laboratory.
‡Research Engineer, Applied Aerodynamics Laboratory.
§Boeing Associate Technical Fellow, Rotorcraft Aerodynamics. Senior Member AIAA.

Because of the Reynolds number of the application (order of millions), the only effective way of producing an aerodynamic database with a reasonable compromise of accuracy and computational costs is to use a RANS methodology. Typically most RANS codes include several turbulence models which have comparable performance and accuracy. The choice of a proper turbulence model depends also on the effectiveness, robustness, and on user confidence for the specific application. Recently, Chi et al. [4] compared three different RANS solvers in the prediction of aerodynamic performance of airfoils with both rime and glace ice formations. Among the various turbulence models studied for glaze ice accretion, the authors obtained the best results in lift prediction with the Spalart–Allmaras (SA) model [for example, over renormalization group theory κ–ε, v^2–f, and a Reynolds stress model (RSM)]. However, for drag prediction, v^2–f and RSM were better. Chung and Addy [5] compared the SA, the Baldwin–Barth one equation, and the shear stress transport (SST) models and obtained the best results with the SA in the case of glaze ice, and SST in the case of rime ice. Progress in the turbulence modeling is achievable by adopting more complex methodologies such as detached eddy simulation (DES) or large eddy simulation (LES). In the work of Pan and Loth [6], the flow around the NLF-0414 and NACA 23012 airfoils with prescribed iced shapes was computed with a DES approach yielding encouraging results, although a systematic convergence and grid parameter study is not yet computationally practical in an industrial environment. In the present work, a detailed comparison of two turbulence models, SA [7] and SST [8], is addressed by using three different RANS codes. This paper is structured as follows: first, the numerical code features are presented and a summary of the CFD grid details are given (Secs. II and III). Then, an assessment of numerical uncertainty, grid convergence, and turbulence model effects among the codes is discussed by focusing attention on the case at $\alpha = 6$ deg (Sec. IV). Finally, the complete aerodynamic characterization, from $\alpha = -4$ to 12 deg, is presented with a description of key flow structures at various angles of attack (Sec. V).

II. Numerical Methods

To assess the numerical uncertainty, three different RANS codes have been compared: ZEN, FLUENT, and CFL3D. ZEN [9], an in-house code developed at CIRA, is a very robust, flexible, and widely tested computational tool for the aerodynamic analyses of complex configurations (including complete aircraft) in subsonic, transonic, and supersonic flow regimes. It solves the Euler and RANS equations (for both steady and unsteady flow simulations) using a multizonal approach with multiblock structured grids. The spatial discretization is based on a cell-centered finite volume formulation, with second- and fourth-order artificial dissipation. The solution procedure adopts the pseudotime marching concept, with the relaxation operator consisting of a multistage Runge–Kutta integration scheme. The pseudotime marching approach obtains the steady-state solution by evolving from an initial guess until convergence is achieved. The convergence toward the solution is accelerated by local time stepping, implicit residual averaging, and a multigrid method. The unsteady computations are carried out by dual time stepping [10]; the physical time derivatives are computed by a second-order accurate formula.

FLUENT [11] is a commercial code based on a finite volume approach with unstructured grids for simulating complex fluid flows, heat and mass transfer, for both steady and unsteady simulations. Although the code provides several models, in the present work a second-order upwind scheme has been adopted for the spatial discretization. Because of the low effects of the compressibility in the experiment [2], an incompressible formulation was chosen as the governing mathematical model, and the energy equation was disregarded.

CFL3D [12] is a general purpose, structured finite volume CFD code developed at the NASA Langley Research Center for solving flows on structured grids. General features of the code include two- or three-dimensional grid topologies, inviscid, laminar, or turbulent flows, and steady or unsteady flows. CFL3D solves for solutions on single or multiple blocks with one-to-one point matched, patched, or overlapped interfaces. Several convergence acceleration options are available including multigrid and mesh sequencing.

Although several turbulence models are available in ZEN, FLUENT, and CFL3D, the Menter's κ–ω SST and SA models are used exclusively in this application. The freestream turbulence measured in the LTPT tunnel was 0.1%. No information about a possible boundary layer transition was available at the time of this work. Thus, in all simulations the codes were run with a fully turbulent condition.

III. Computational Grid

The 623-2D iced shape assigned on the NLF-0414 airfoil is a typical glaze shape with a double horn at the leading edge. Residuals of ice are also present on the lower surface of the airfoil. To reduce sources of uncertainty associated with the geometry and the discretization, a unique computational grid with a *C*-type topology was generated and used by all three codes. The initial defining geometry representing the iced airfoil was fit with a smooth interpolating (analytic) spline to create a refined computational surface. The grid is 1665×289 on the finest level with 1281 points on the airfoil surface and 193 points along the wake cut. Grid lines are clustered normal to the airfoil surface to target a y^+ of order 1. Two hundred eight-nine grid points are used to stretch the mesh to the far field 30 chord lengths away. A comprehensive view is given in Fig. 1 along with a close-up near the upper leading edge. The dense discretization near the horn is motivated by the presence of a strong

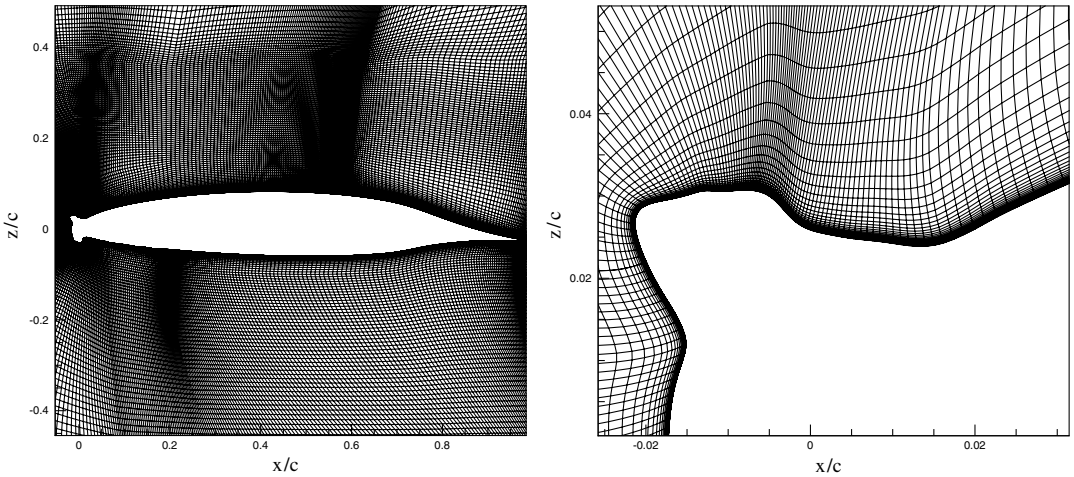

Fig. 1 A comprehensive view (left) and details near the leading edge (right) of the CFD grid. Every other grid line is shown in both computational directions for clarity.

shear layer between the external stream and the expected recirculation bubble just behind the horn. The grid was optimized to operate at $\alpha = 6$ deg; however, it was used throughout the range of angles of attack studied. Further improvements are possible for higher angles of attack. In fact, for $\alpha = 8$ through 12 deg using the ZEN code with the SA model, a slight modification of the grid was introduced to improve the convergence.

IV. Numerical Case Setup

Numerical results from three different codes and two turbulence models are presented by comparing solutions for an angle of attack sweep at Mach 0.21 ($Re = 4.6 \times 10^6$). Though the codes are using the same computational grid and are solving fundamentally the same equations with the same boundary conditions, the uniqueness of the solution is not assured. Differences in the solutions can be expected because the codes use different numerical schemes with different dissipation properties. The issue is compounded by the turbulence modeling. Though the models are nominally the same, their implementations differ. To understand the sensitivity of the numerous parameters involved, an effort to identify the sources of uncertainty was pursued. In the following, three aspects are considered: the grid dependency, the turbulence modeling, and the numerical dissipation.

A. Grid Dependency

The numerical solutions show a significant dependency on the grid refinement, especially for the highest angles of attack. The effects of grid dependency are apparent in terms of lift and drag coefficients from $\alpha = -4$ to 6 deg, where residual convergence has been obtained on each grid level by all codes. Coarser grid levels have been obtained by removing every other grid line. Richardson's extrapolation was applied to the results on the last two levels, labeled as medium and fine. As can be seen in Fig. 2, the lift coefficient increases its grid dependency by increasing the angle of attack. Comparisons of the c_d show a lower sensitivity. Of all the codes, ZEN exhibits the highest grid dependency. In particular, the change in c_l between the medium and fine levels has an approximately linear increase in slope, whereas the others two codes seem to be quite insensitive. The most likely reason for the behavior noted in the ZEN results is its utilization of the scalar dissipation model of Jameson et al. [13]. Swanson et al. [14] observed a strong sensitivity of the scalar dissipation model to grid resolution when applied to situations involving a viscous boundary layer. In the present case, the thickness of the viscous layer is proportional to the separation bubble dimension that grows with angle of attack. By considering the grid convergence trend of the pressure coefficient distribution at $\alpha = 6$ deg, shown in Fig. 3 from the coarsest to the finest grid, the major variations appear on the upper side of the airfoil. This confirms the hypothesis that the discrepancies are associated with the extension of the separated flow zones. Near the trailing edge the numerical results capture the experimental pressure level satisfactorily. The solution on the lower side is quite insensitive to grid refinement, although some small effects can be noted. Only grid dependency results for the SST model are reported as analogous conclusions apply for the SA model.

B. Turbulence Models

Literature recognizes significantly different behavior of turbulence models in computing flows around iced airfoils [4–6]. This is confirmed in the present work where the SST model is compared with the SA model. The effects of the turbulence models are clearly visible in the comparison of the pressure distributions shown in Fig. 3. The key point is demonstrated by the separation layer developing downstream of the upper horn. The turbulence models predict substantially different expansion levels, yielding an improbable flow evolution on the upper surface. This is associated with the lack of consistency in the turbulence models for predicting reverse flow properties such as the bubble forming at the leading edge. The SA model produces higher expansions near the leading edges that are closer to the experiments than the SST results. This behavior is systematically confirmed for each angle of attack and for each of the three RANS codes (c_p distributions for other angles of attack are shown in Sec. V). Consequently, it can be considered as a property of the SA turbulence model itself. This is in agreement with the work of Chung and Addy [5] who obtained better results with the SA model in the case of glaze ice accretion.

C. Dissipation Properties of Codes

Once the geometry and the boundary conditions are fixed, the discrepancies among the numerical results are due to the convergence levels, the dissipative properties of the numerical scheme, or the turbulence modeling. In the present work, a fully steady convergence has been achieved for angles of attack up to $\alpha = 6$ deg in each simulation, indicating that the iterative convergence errors for such solutions are negligible. With discrepancies in turbulence minimized (or eliminated) by fixing the turbulence models, the discrepancies among the solutions are directly associated with the dissipative properties of the numerical scheme used. By analyzing the flowfield produced by the three codes at $\alpha = 6$ deg, the regions where the discrepancies arise can be identified. In Figs. 4a, 4c, and 4e, the field of the u component of velocity (parallel to the chord) is shown for each code, whereas in Figs. 4b, 4d, and 4f the absolute difference field of the u component of velocity among the three CFD codes is shown. The SA model is presented for discussion. A six level gray-scale map is plotted starting from 0.05 to 0.5 with a delta of 0.09. The values are dimensionless with respect to the freestream velocity. The white areas correspond to the regions where the discrepancies are less than 0.05, and the black areas correspond to where the differences are more than 0.5. In Fig. 4b, the main discrepancies in $|\Delta u|$ are concentrated on the upper airfoil side. The maximum value is about 0.2 and is located in the proximity of the reattachment of the

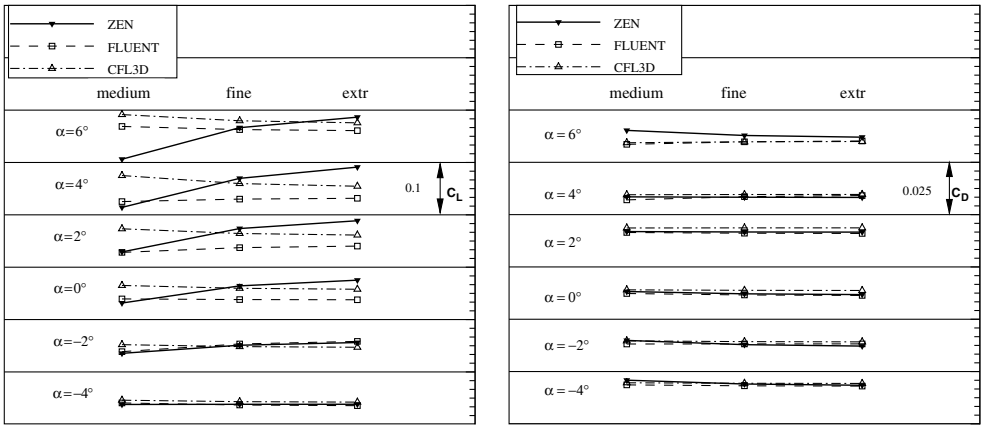

Fig. 2 Grid convergence effects on c_l (left) and c_d (right) for ZEN, FLUENT, and CFL3D using the SST model.

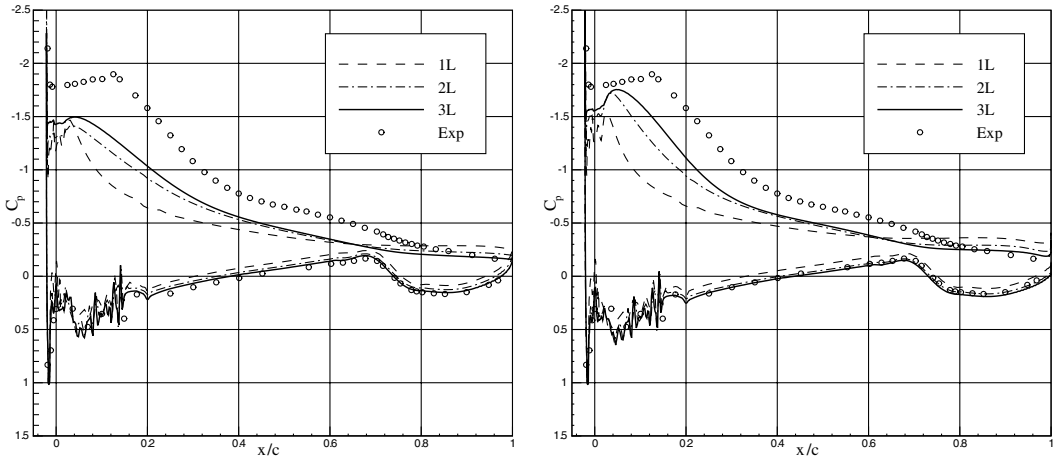

Fig. 3 Grid convergence effects on c_p at $\alpha = 6$ deg for ZEN using the SST model (left) and SA model (right). 1L: coarse; 2L: medium; 3L: fine grid level.

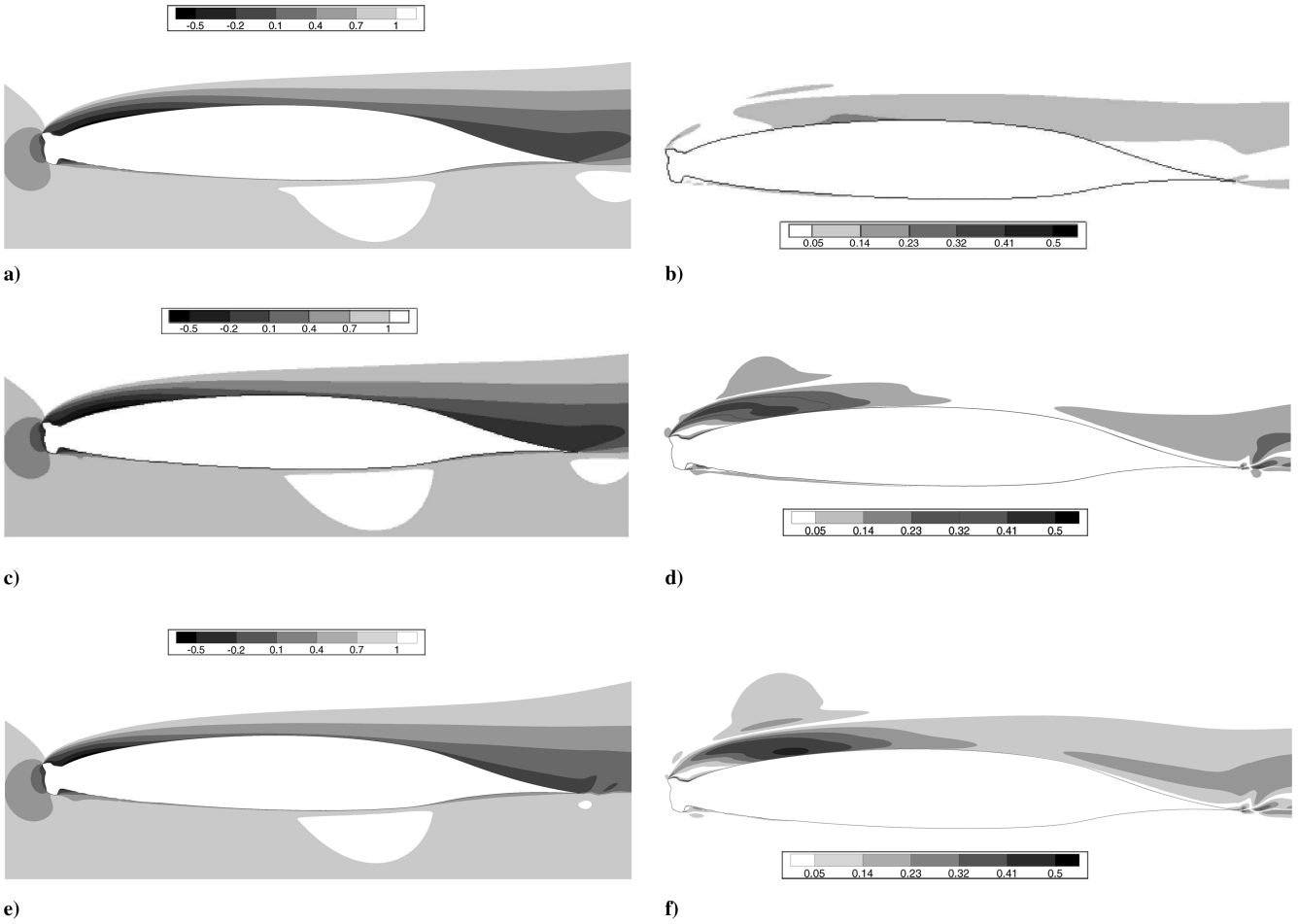

Fig. 4 a) The u component at $\alpha = 6$ deg from the ZEN solution. b) $|\Delta u|$ between ZEN and FLUENT. c) The u component at $\alpha = 6$ deg from the FLUENT solution. d) $|\Delta u|$ between FLUENT and CFL3D. e) The u component at $\alpha = 6$ deg from the CFL3D solution. f) $|\Delta u|$ between CFL3D and ZEN.

separation bubble directly behind the horn. Between this bubble and the trailing-edge separation, the velocity is in good agreement (<0.05). A gray area (0.05–0.14) covers a region 0.06c high. In Fig. 4d the differential field is computed by using FLUENT (Fig. 4c) and CFL3D (Fig. 4e) results. An area of discrepancy (0.32–0.41) arises corresponding to the reattachment zone. Over the middle of the chord the agreement is satisfactory (<0.05), but near the leading edge a gray region (0.05–0.14) appears. In Fig. 4f, the differences concern CFL3D (Fig. 4e) and ZEN (Fig. 4a). The darkest area is concentrated near the reattachment point of the separation bubble. In this zone, the discrepancies are greater than 0.5. The agreement is satisfactory (<0.05) only inside the leading-edge bubble. Globally, a gray area (0.05–0.14) is confined to a region whose thickness increases from 0.06c at the midchord to 0.08c at the trailing edge. Thus, it is possible to conclude that the major discrepancies are confined to a region (0.06–0.08)c thick above the airfoil. The most critical point is in the separation layer arising from the leading-edge upper horn. From there, a different flow evolution is determined

which influences the field downstream. The actual numerical discrepancies are attributed to the dissipative properties of the schemes used in each code. ZEN uses a central scheme with an explicit artificial viscosity model whereas FLUENT uses a second-order upwind discretization scheme with an implicit segregated solver and the SIMPLE pressure-velocity coupling algorithm. CFL3D was run using Roe's third-order upwind-biased flux difference splitting scheme. The different dissipative properties in each code generate different results for the same turbulence model. Finally, the numerical discrepancies evidenced from this analysis appear in the zones where the agreement with the experimental data is poorer (shown in more detail in Sec. V).

V. Result Discussion

A. Global Aerodynamic Coefficients

Hereafter, only the extrapolated coefficients to an infinite mesh are considered. Figure 5 shows the lift curve plotted against the angle of attack. For $\alpha \leq 0$ deg the experimental slope is well captured by all codes, though results computed with the SST model have a greater spread than the SA results. With the SST model the predicted stall angle is about 6 deg though ZEN results stall slightly sooner than the others. After the stall, each numerical code demonstrates a different behavior but these calculations are compromised by lower convergence levels and by the breakdown of turbulence model effectiveness in such conditions. In general, the c_l computed with the SA model is higher than SST results, and the agreement with the experiments improves. In Fig. 6 the drag results are shown for the SST and SA models. The numerical results are shown up to $\alpha = 6$ deg because of the absence of experimental information for greater angles. The slope of the numerical curves follows the experimental trend up to $\alpha = 2$ deg. For $\alpha \geq 4$ deg the c_d is underestimated. The spread of the numerical results is approximately the same for both turbulence models. In Fig. 7 the pitching moment coefficients c_m are plotted as a function of α. In this case no experimental information is available. The c_m provides an indication of the pressure distribution along the airfoil. The agreement among the codes is satisfactory up to $\alpha = 6$ deg, beyond which the separation becomes extensive.

B. Pressure Coefficient Distributions

The pressure coefficients along the airfoil contour are plotted for each code and for both turbulence models starting from $\alpha = -4$ to 10 deg (see Figs. 8–15). At $\alpha = -4$ deg, the upper airfoil surface is subject to a compression whose peak is well predicted by all codes. Small discrepancies with the SA model appear near the leading edge on both lower and upper sides. At $\alpha = -2$ deg, near the leading edge, some uncertainties are visible among the codes. At $\alpha = 0$ deg, the numerical c_p distributions of the SST models are very similar among the three codes, even if the expansion on the upper side is underestimated with respect to the experimental data. The SA model has the same behavior, except near the leading edge on both upper and lower sides, where the codes predict different pressure levels. The oscillations in c_p on the lower side are due to the jagged contour

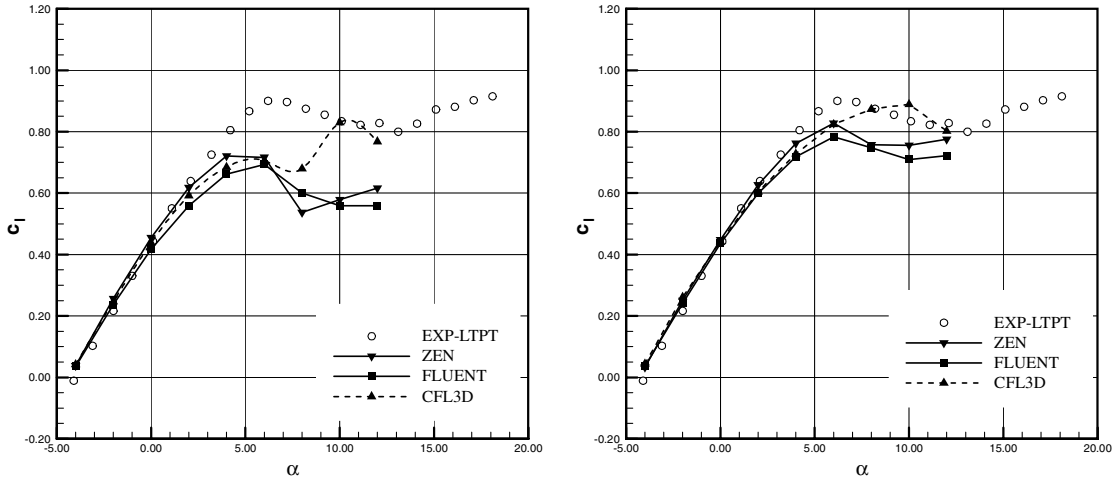

Fig. 5 The c_l–α curve for the SST model (left) and SA model (right).

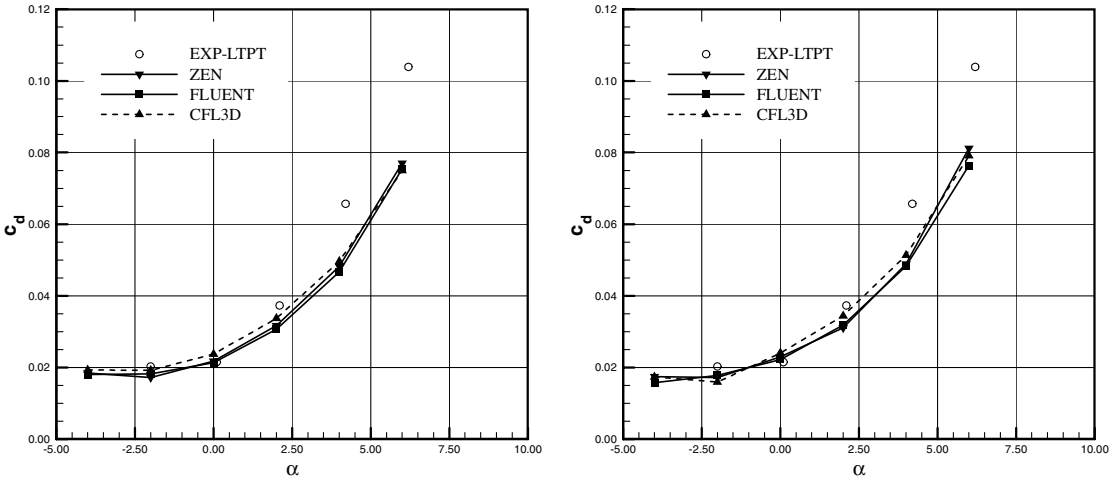

Fig. 6 The c_d–α curve for the SST model (left) and SA model (right).

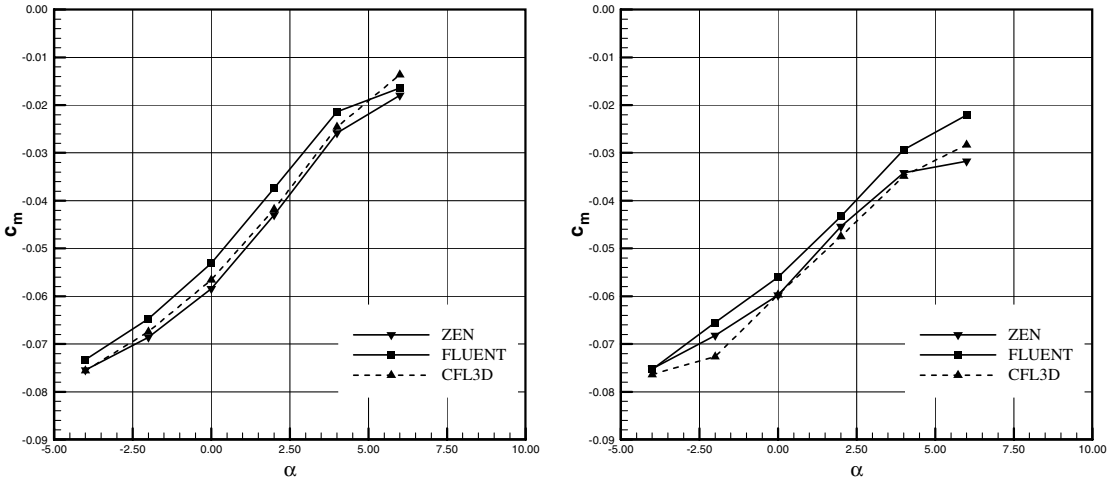

Fig. 7 The c_m–α curve for the SST model (left) and SA model (right).

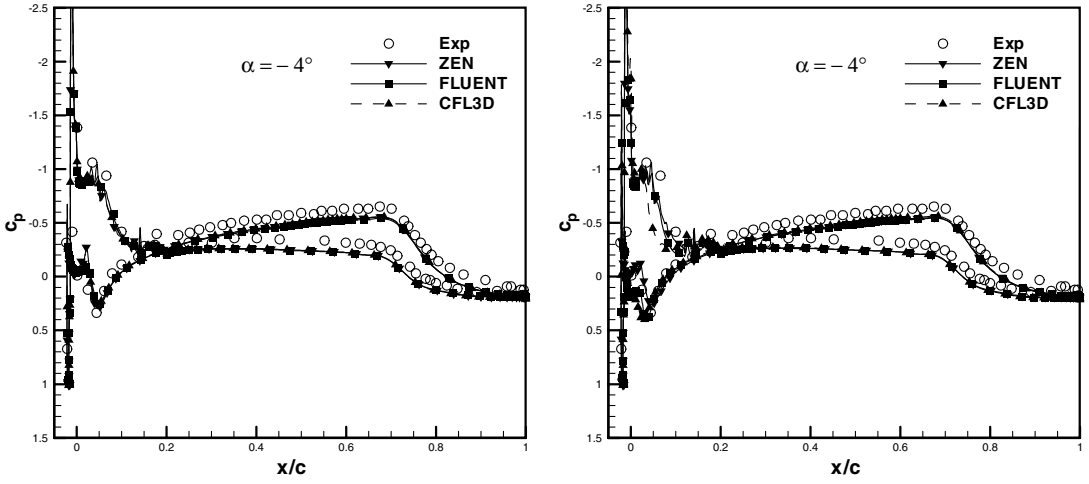

Fig. 8 The c_p distributions at $\alpha = -4$ deg for the SST model (left) and SA model (right).

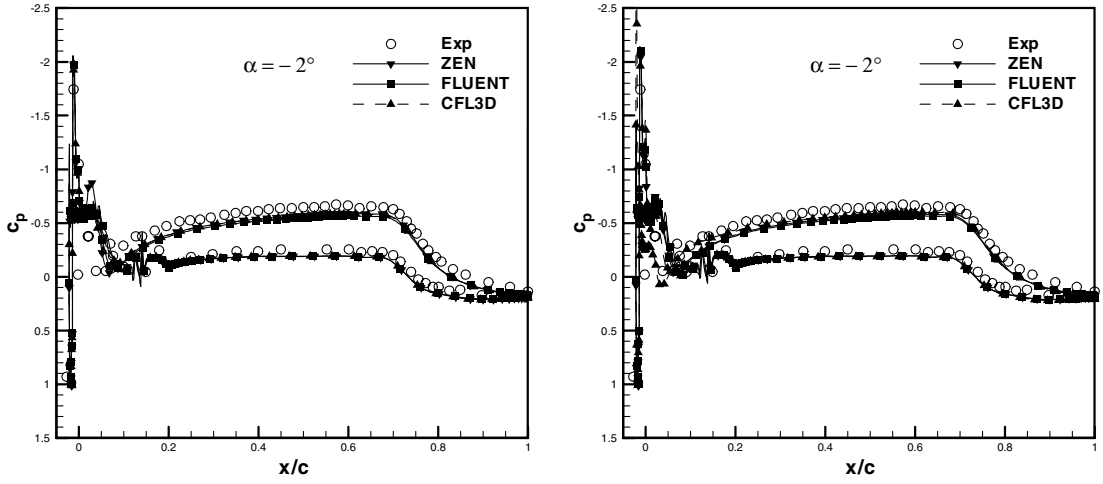

Fig. 9 The c_p distributions at $\alpha = -2$ deg for the SST model (left) and SA model (right).

representing residual ice accumulation. At $\alpha = 2$ deg, the SST results are in reasonably good agreement, but differ substantially with the experimental values. In particular, the expansion peak on the upper side is underestimated. The SA solutions exhibit an expansion peak close to the experimental value, but the subsequent pressure recovery is not well defined. At $\alpha = 4$ deg, the SST results underpredict the experimental levels on the complete upper side. The SA model captures the level of the expansion peak, but underestimates the pressure recovery. Conversely, the c_p on the lower side is satisfactorily predicted by both the turbulence models. At $\alpha = 6$ deg, the expansion peak increases, but the SST results still underestimate the experimental value. The SA results, on the other

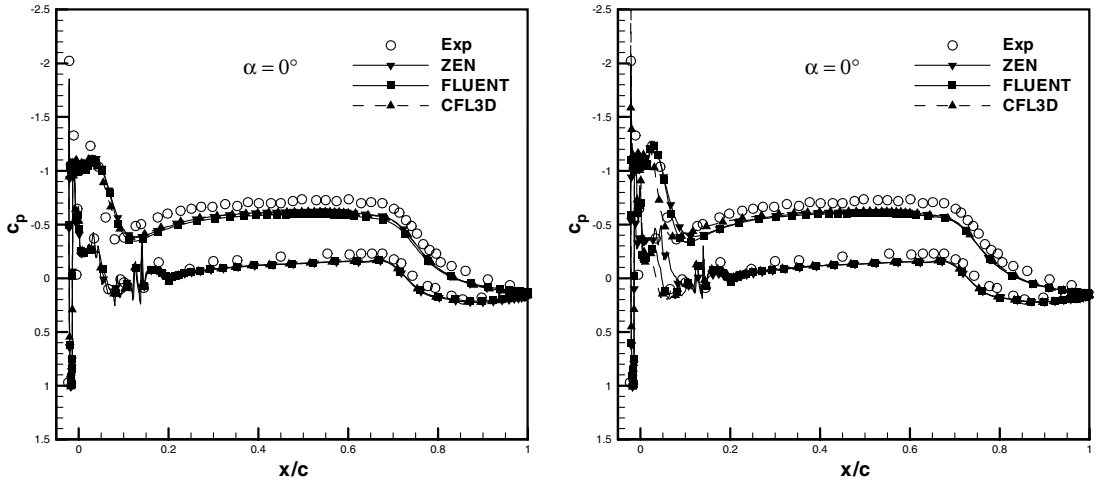

Fig. 10 The c_p distributions at $\alpha = 0$ deg for the SST model (left) and SA model (right).

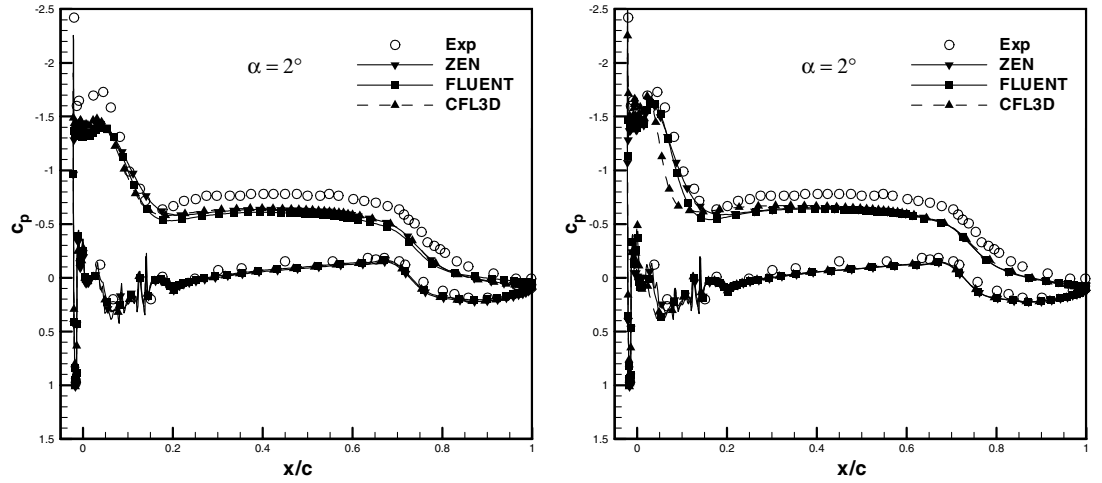

Fig. 11 The c_p distributions at $\alpha = 2$ deg for the SST model (left) and SA model (right).

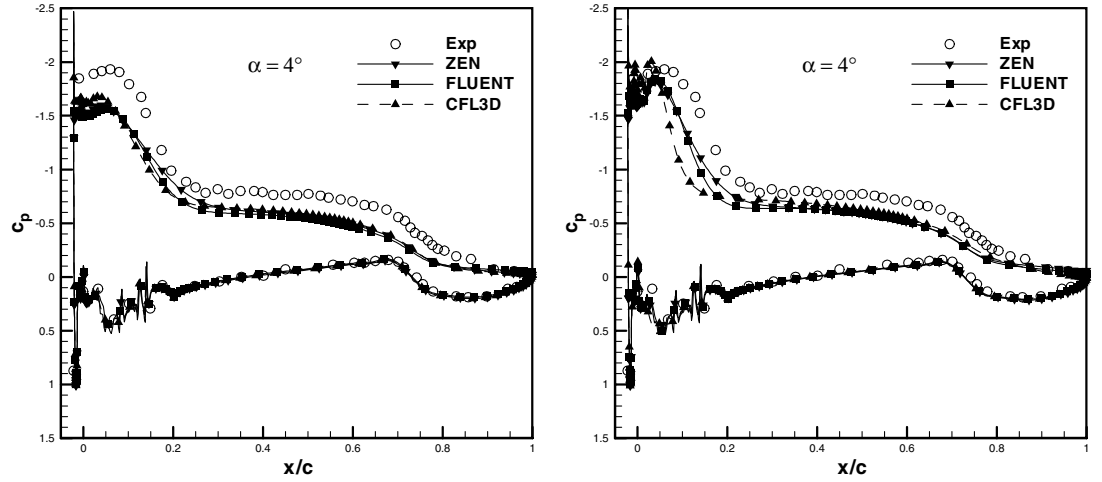

Fig. 12 The c_p distributions at $\alpha = 4$ deg for the SST model (left) and SA model (right).

hand, demonstrate an expansion peak greater than SST, even if the pressure recovery downstream is far from the experimental values. CFL3D generates the highest expansion peak for both the turbulence models. At $\alpha = 8$ deg, SST results are significantly below the experimental curve. Analogous considerations are applicable for the case at $\alpha = 10$ deg.

C. Flow Topology

The flow around the NLF-0414 at moderate angles of attack (i.e., $\alpha \leq 6$ deg) is characterized by the presence of two recirculation bubbles and a trailing-edge separation. As shown in Fig. 16, the bubbles are labeled as B_1 and B_2 and their reattachment locations are x_1 and x_2, respectively. The trailing-edge separation is indicated by

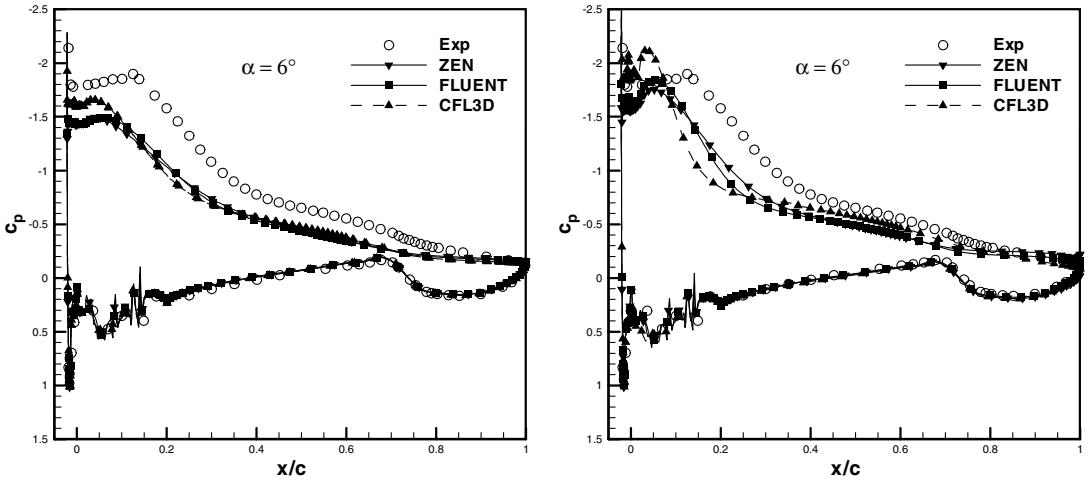

Fig. 13 The c_p distributions at $\alpha = 6$ deg for the SST model (left) and SA model (right).

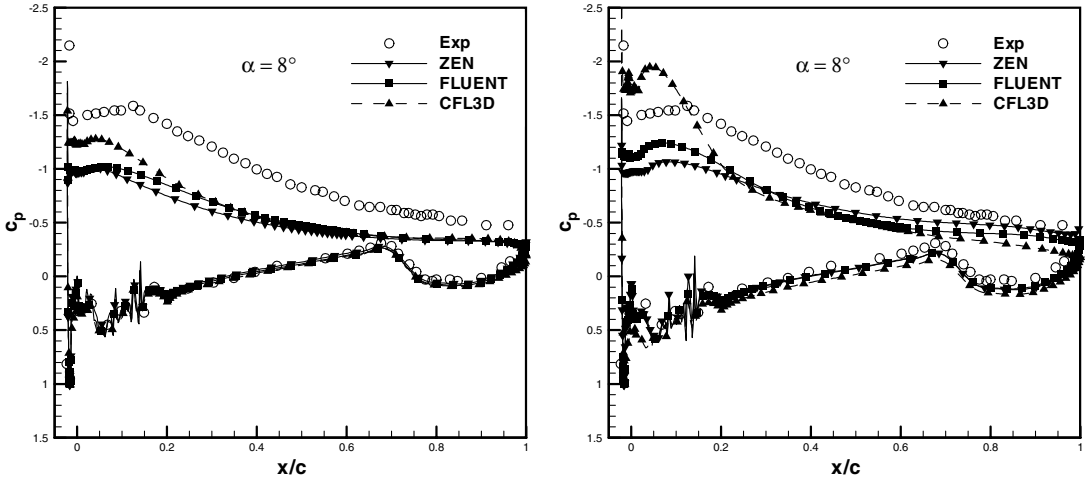

Fig. 14 The c_p distributions at $\alpha = 8$ deg for the SST model (left) and SA model (right).

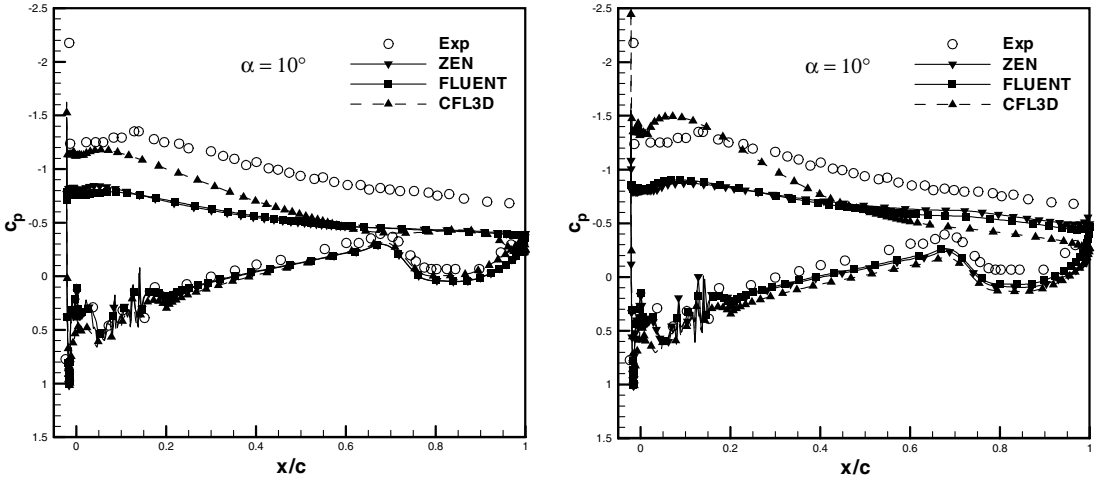

Fig. 15 The c_p distributions at $\alpha = 10$ deg for the SST model (left) and SA model (right).

x_s. Such abscissas are measured along the chord. B_1 is located just aft of the leading-edge ice on the upper surface. In this region, the separation is geometrically induced by the iced protuberances and it is essentially independent on flow properties. B_1 is placed where the flow expands as can be seen in the c_p distributions. A severe shear layer occurs between the external flow and the reverse flow of B_1 enhancing the production of turbulent kinetic energy. B_2 is on the lower airfoil surface and has smaller dimensions than B_1. Full separation arises when $x_1 \geq x_s$. The numerical results indicate that this occurs for $\alpha \geq 8$ deg. In Fig. 17, x_1, x_2, and x_s are plotted as functions of angle of attack. It can be noted that x_1 grows proportionally to α^2, whereas x_2 decreases approximately with a

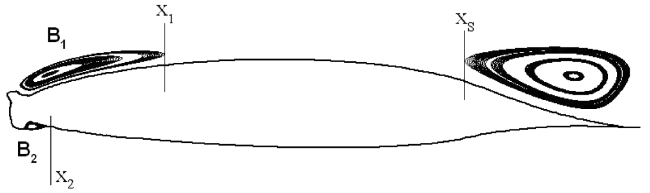

Fig. 16 Reattachment and separation abscissas.

linear law. More uncertainties arise when the x_s results are considered. In particular, for the SST data, FLUENT yields a slight separation even at $\alpha = 2$ deg, whereas CFL3D and ZEN separate at $\alpha = 4$ deg. Yet, with the SA model, CFL3D anticipates the separation at $\alpha = 0$ deg, whereas with ZEN and FLUENT it appears at $\alpha = 2$ deg. Thus, the turbulent separation x_s is rather uncertain, and no experimental information is available to support the reliability of the actual numerical results. In Fig. 18 the streamlines obtained by ZEN at angles of attack up to 6 deg are shown. A completely separated flow arises for $\alpha \geq 8$ deg. Beyond this angle, the steady convergence degrades, even if it has been achieved for most of the cases.

Poorer iterative convergence is due to the massively separated flow regions arising in the wake that have a marked unsteady behavior [15–18]. Even if the RANS models advance in time accurately, there is no guarantee that such unsteadiness is resolvable. In fact, when the unsteady solver has been used for the conditions $\alpha = 8$–12 deg, a steady state or weakly oscillating solutions have been obtained. In any case, no significant unsteadiness has been recognized. However, in some cases, the unsteady procedure has been useful to improve the convergence with respect to the steady one. Nevertheless, it is possible that for the highest angles of attack, a more appropriate computational grid can be designed, and that more accurate methodologies for the turbulence can be employed, such as DES or LES. In the present analysis, three-dimensional effects, always present in a real turbulent flow, have not been taken into account.

VI. Conclusions

An aerodynamic analysis of the NLF-0414 airfoil has been presented. Three different RANS solvers have been used to compare two turbulence models: Menter's κ–ω SST and the Spalart–Allmaras model. The comparisons focus on Mach 0.21 flow over a range of angles of attack from $\alpha = -4$ deg to poststall at $\alpha = 12$ deg. Attention has been paid to assess the numerical uncertainties among the codes. A single computational grid has been used (except for ZEN with the SA turbulence model at poststall conditions) in order to have uniform comparisons. A grid resolution analysis has been performed by obtaining a sequence of solutions on coarser grid levels and by analyzing the grid dependency of some parameters. The numerical spread among the codes grows as α increases. This is attributed, in part, to larger separated zones. Different dissipation properties have been observed by comparing the solutions at $\alpha = 6$ deg. The major discrepancies are confined to a region of thickness between 0.06 and 0.08 chord lengths along the upper side of the airfoil. After the stall, each code shows a different behavior even if the same turbulence model has been used. This is probably attributable to different dissipative properties of the codes. The comparison with experimental data indicates that the SA model yields better results than the SST in lift prediction, as found by Chung and Addy [5] in 2000. The disagreement increases as the angle of attack augments. The SST model almost always underestimates the expansion region near the leading edge. In this regard, the SA model matches the experiments better but exhibits the same loss of accuracy in the recovery pressure zone. On the lower side, instead, the pressure

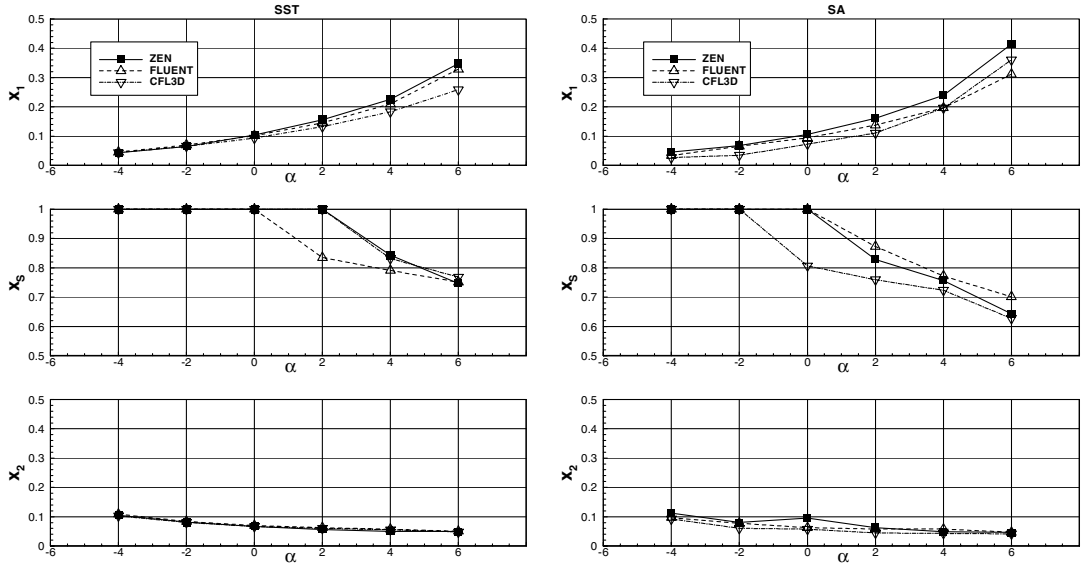

Fig. 17 x_1, x_s, and x_2 abscissas plotted at different angles of attack for the SST model (left) and SA model (right).

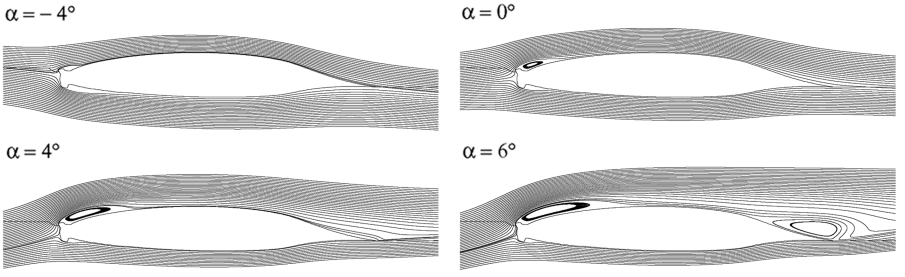

Fig. 18 Streamlines predicted by the ZEN code using the SST model.

coefficient is well predicted by both models. An analysis of the flow topology has been also carried out. Two bubbles and a trailing-edge separation characterize the flow up to $\alpha = 6$ deg. Above this angle of attack, a fully separated region arises on the upper side. A strong shear layer occurs between the upper surface leading-edge bubble and the external flow. The production of turbulent kinetic energy determines the flow reattachment location and, as a consequence, the pressure distribution on the upper surface of the airfoil. It has been found that the upper surface reattachment location grows as α^2; on the lower surface the reattachment location decreases with angle of attack. No uniform results have been obtained concerning the starting location of the upper surface separation region. Fully steady convergence has been obtained for all computations up to $\alpha = 6$ deg. Beyond it, the convergences of the steady solvers degrade. In some cases, an unsteady procedure has been adopted to advance in the convergence process. Nevertheless, even using an unsteady procedure, no relevant unsteadiness has been recognized. Advances in the physical descriptions are possible if newer turbulence methodologies are employed, such as DES or LES, though larger computational costs will be required.

Acknowledgment

Elements of the activity presented here have been carried out within the project ACADEMIA (Advanced Computational Aerodynamic Environment for Multidisciplinary Integrated Analysis) partially funded by the Italian Ministry for University and Scientific Research.

References

[1] Mingione, G., Zanazzi, G., Brandi, V., Hartman, P., Narducci, R., Peterson, A., and Dadone, L., "Prediction of Ice Accumulation and Airfoil Performance Degradation: A Boeing—CIRA Research Collaboration," *American Helicopter Society 62nd Annual Forum Proceedings*, 9–11 May 2006.

[2] Addy, H. E., and Chung, J. J., "A Wind Tunnel Study of Icing Effects on a Natural Laminar Flow Airfoil," AIAA Paper 2000-0095, 10–13 Jan. 2000.

[3] Addy, H. E., "Ice Accretions and Icing Effects for Modern Airfoils," NASA TP 2000-210031, April 2000.

[4] Chi, X., Li, Y., and Chen, H., "A Comparative Study Using CFD to Predict Iced Airfoil Aerodynamics," AIAA Paper 2005-1371, 10–13 Jan. 2005.

[5] Chung, J. J., and Addy, H. E., "A Numerical Evaluation of Icing Effects on a Natural Laminar Flow Airfoil," NASA TM-2000-209775, Jan. 2000.

[6] Pan, J., and Loth, E., "Detached Eddy Simulations for Iced Airfoils," *Journal of Aircraft*, Vol. 42, No. 6, 2005, pp. 1452–1461. doi:10.2514/1.11860

[7] Spalart, P. R., and Allmaras, S. R., "A One Equation Turbulence Model for Aerodynamic Flows," AIAA Paper 1992-0439, 6–9 Jan. 1992.

[8] Menter, F. R., "Two Equation Eddy Viscosity Turbulence Models for Engineering Applications," *AIAA Journal*, Vol. 32, No. 8, 1994, pp. 1598–1605.

[9] Catalano, P., and Amato, M., "An Evaluation of RANS Turbulence Modeling for Aerodynamics Applications," *Aerospace Science and Technology*, Vol. 7, No. 7, Oct. 2003, pp. 493–509. doi:10.1016/S1270-9638(03)00061-0

[10] Jameson, A., "Time-Dependent Calculations Using Multigrid, with Application to Unsteady Flows Past Airfoils and Wings," AIAA Paper 1991-1596, 24–26 June 1991.

[11] Fluent 6.1, User's Guide, Feb. 2003.

[12] Thomas, J. L., Anderson, W. K., and Krist, S. T., "Navier-Stokes Computations of Vortical Flows Over Low-Aspect-Ratio Wings," *AIAA Journal*, Vol. 28, No. 2, 1990, pp. 205–212.

[13] Jameson, A., Schmidt, W., and Turkel, E., "Numerical Solutions of the Euler Equations by Finite Volume Methods Using Runge-Kutta Time Stepping Schemes," AIAA Paper 1981-1259, 23–25 June 1981.

[14] Swanson, R. C., Radespiel, R., and Turkel, E., "On Some Numerical Dissipation Schemes," *Journal of Computational Physics*, Vol. 147, No. 2, Dec. 1998, pp. 518–544. doi:10.1006/jcph.1998.6100

[15] Bragg, M. B., Khodadoust, A., and Spring, S. A., "Measurements in a Leading-Edge Separation Bubble due to a Simulated Airfoil Ice Accretion," *AIAA Journal*, Vol. 30, No. 6, June 1992, pp. 1462–1467.

[16] Broeren, A. P., and Bragg, M. B., "Low-Frequency Flow Field Unsteadiness During Airfoil Stall and the Influence of Stall Type," AIAA Paper 1998-2517, 15–18 June 1998.

[17] Broeren, A. P., and Bragg, M. B., "Spanwise Variation in the Unsteady Stalling Flow Fields of Two-Dimensional Airfoil Models," *AIAA Journal*, Vol. 39, No. 9, Sept. 2001, pp. 1641–1651.

[18] Zaman, K. B. M. Q., McKinzie, D. J., and Rumsey, C. L., "A Natural Low Frequency Oscillation of the Flow Over an airfoil Near Stalling Conditions," *Journal of Fluid Mechanics*, Vol. 202, May 1989, pp. 403–442. doi:10.1017/S0022112089001230

R. So
Associate Editor